A Combined Computational and Experimental Study of Ion-Beam Modification of Carbon Nanotube Bundles

Boris Ni,[†] Rodney Andrews,[‡] David Jacques,[‡] Dali Qian,[‡] Muthu B. J. Wijesundara,[§] Yongsoo Choi,[§] Luke Hanley,[§] and Susan B. Sinnott*,[†]

Department of Materials Science and Engineering, The University of Florida, Gainesville, Florida 32611-6400, Center for Applied Energy Sciences, The University of Kentucky, Lexington, Kentucky 40511, and Department of Chemistry, The University of Illinois at Chicago, Chicago, Illinois 60607-7061

Received: June 19, 2001

The modification of bundled single-walled and multiwalled carbon nanotubes is examined using a combination of computational and experimental methods. The computational approach is classical molecular dynamics simulations using the many-body reactive empirical bond-order potential parametrized by Brenner. The simulations consider the deposition of CH_3^+ at incident energies of 10, 45, and 80 eV. They predict the chemical functionalization of the nanotubes, the formation of defects on the nanotube walls, and the formation of cross-links between neighboring nanotubes or between the walls of a single nanotube. They also illustrate the manner in which the number of walls in the nanotube and incident energy affect the results. In the experiments, multiwalled nanotubes with about 40 shells (average diameter of 25 nm) are synthesized by chemical vapor deposition. CF_3^+ ions are deposited at incident energies of 10 and 45 eV, and then the nanotubes are examined with X-ray photoelectron spectroscopy and scanning electron microscopy. These experiments find strong evidence of chemical functionalization, in agreement with the simulation results.

Introduction

Nanotubes have unique mechanical and electrical properties that make them ideal candidates for the creation of nanometer-scale devices and new composite materials. For example, depending on their helical structure, nanotubes can exhibit metallic or semiconducting conductivity.[1] Semiconducting nanotubes can function as field-effect transistors,[2,3] while metallic nanotubes can function as single electron transistors.[4,5] Nanotubes are also being considered for use as fibers for the next generation of composite materials because of their unusual anisotropic mechanical properties (extreme stiffness in the axial direction and great flexibility in the direction perpendicular to the axial direction).[6−8]

To fully exploit their remarkable properties in technological applications, it is often necessary to modify them from the as-processed state.[9−13] One possible modification is chemical functionalization of the nanotube walls so that their adhesion to the polymer matrix in a composite can be varied or so that electrical junctions between nanotubes in nanometer-scale electrical circuits can be made. Existing methods of chemical functionalization[14−21] of nanotubes depend on chemical procedures such as carbodiimide chemistry or mixing the nanotubes with an electrophilic reagent that adds to deactivated double bonds.

In our previous computational study,[22] polyatomic ion bombardment is predicted to be an effective method of chemical functionalization of single-walled nanotubes (SWNTs) arranged in a bundle at low and medium incident energies of 10−45 eV. In addition, bombardment at higher incident energies of 80 eV is predicted to lead to cross-linking between the nanotubes in certain instances.[22] Nanotube junctions[23−30] have also attracted much attention because they represent the most basic possible electrical circuit. However only two kinds of junctions have been studied in the literature so far: end-to-end connection of SWNTs of different chirality through a connecting layer of pentagon−heptagon defects[23−27] and crossing nanotubes by putting them on top of one another separated by the regular van der Waals separation distance.[28−30]

In this paper, we extend our previous study of functionalization and modification of SWNTs to multiwalled nanotubes (MWNTs) and explore the possibility of their connectivity by ion bombardment using a combination of experimental and computational methods.

Experimental Details

Carbon Nanotube Synthesis. The synthesis of MWNTs proceeds by reacting hydrocarbon vapor over a dispersed iron catalyst that is deposited in situ in a quartz tube reactor within a multizone furnace.[31] A xylene−ferrocene feedstock is continuously injected via syringe pump into a preheat section operated at ∼250 °C. The xylene−ferrocene vapors are swept into the reaction zone of the furnace by an Ar/10% H_2 carrier gas that also maintains a partial pressure of 32 mbar of carbon inside the reactor. The reaction zone is held at 725 °C with an Ar/H_2 flow rate of 6 L/min (STP). A quartz plate is placed within the reactor to provide a support for several 2.5 cm by 2.5 cm plaques of silicon wafer. The reactor is purged, the xylene−ferrocene feed is started, and the reaction is allowed to proceed for 2 h. Upon completion, the xylene−ferrocene feed is stopped, and the reactor is allowed to cool to room temperature under flowing argon. Once cooled, the reactor is opened, and the silicon substrates (now coated with aligned MWNT) are recovered. The

* To whom correspondence should be addressed. E-mail: sinnott@mse.ufl.edu. Tel: 352-846-3778.
[†] The University of Florida.
[‡] The University of Kentucky.
[§] The University of Illinois at Chicago.

10.1021/jp0123233 CCC: $20.00
Published on Web 11/02/2001

product consists of dense arrays of well-aligned multiwalled carbon nanotubes with about 40 shells, typically 25−30 nm in diameter and 50 μm in length. The MWNTs contain ~6% residual iron catalyst within the nanotube cores, but no cogenerated disordered carbon is detectable in scanning electron microscopy (SEM) analysis.

Functionalization and Characterization. The ultra-high-vacuum apparatus used to modify and analyze the nanotube samples has been described previously.[32] This apparatus has a differentially pumped, low-energy ion source for production of mass-selected CF_3^+ ion beams in a preparation chamber and an analysis chamber in which X-ray photoelectron spectroscopy is performed. CF_3^+ ions are produced by electron impact ionization of C_3F_6 gas and then mass-selected by a Wien filter and steered by ion optics onto the sample. The ions impact with either 10 or 45 eV of kinetic energy at normal incidence onto the nanotube sample that is mounted in the preparation chamber. Two CF_3^+ ion fluences are used, either the regular dose of 5×10^{15} ions/cm^2 or the high dose of 1×10^{16} ions/cm^2. Freshly CF_3^+ ion-modified nanotube samples are then transferred in situ and without any air exposure to the analyzing chamber for X-ray photoelectron spectroscopy (XPS) analysis.

Details of the XPS experiments and data analysis are similar to those employed previously and are only summarized here.[32,33] XPS is performed with a high-resolution monochromatic Al Kα X-ray source (15 keV, 25 mA emission current, model VSW MX10 with 700 mm Rowland circle monochromator, VSW Ltd., Macclesfield, Cheshire, U.K.) and a 150 mm concentric hemispherical analyzer (model class 150, VSW Ltd.) with multichannel detector operated at constant energy analyzer mode. The photoelectron takeoff angle is normal to the surface, and the pass energy of the electron energy analyzer is 22 eV, which gives a 0.75 eV energy resolution for the Ag ($3d_{5/2}$) peak on a clean Ag foil. The C(1s) (aromatic) core level peak of the native nanotubes is assigned to 285.0 eV and is used as a reference for all other photoemission peaks. Curve fitting of the C(1s) spectra is performed using the Spectra software (VSW) with Shirley background and 35:65 Lorentzian:Gaussian product line shapes of variable widths. Atomic concentration percentages are determined from the C(1s) and F(1s) peak areas, taking into account elemental sensitivity factors[34] and the transmission function for the electron energy analyzer (VSW).

Computational Details

The computational approach used is classical molecular dynamics with a time step of 0.20 fs. The interatomic potential used is the analytic reactive empirical bond-order potential of Abel−Tersoff that has been parametrized for hydrocarbons by Brenner and is coupled to long-range Lennard-Jones potential.[35,36] This many-body potential has been shown to be qualitatively good at modeling related processes such as ion deposition on polymer surfaces[32,33] and the mechanical properties of carbon-based materials.[6,37−39] However, as is the case for all empirical potentials, there are cases in which the quantitative accuracy is lacking even while the qualitative trends are correct. For example, it has been shown that this potential predicts association potentials for H + CH_3 and H + diamond (111) that are significantly smaller than ab initio values because of the potential's shorter range.[40] Nevertheless, within the potential cutoff, the predicted association potentials are similar to the ab initio values. Therefore, this effect is not of significant concern in the present study because of the relatively high incident energies used that bring the incident ions into close contact with the nanotube walls (well within the potential cutoff) prior to any reaction. An additional point to be made about the Brenner potential is that it does not include electronic effects such as electronic excitations or charging of the atoms. Therefore, the potential treats ions with positive charges as radicals rather than true ions with an actual positive charge. It is recognized that the presence of a positive charge will influence the chemical reactions that will occur during deposition. However, it is also recognized that many of the ions will be rapidly neutralized as they approach the surface. The expectation is that the simulation results are qualitatively correct and can provide insight into the processes taking place during ion-beam modification of nanotubes.

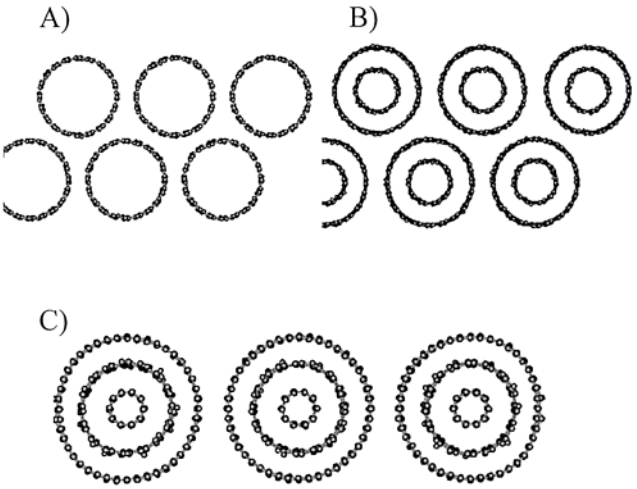

Figure 1. Initial configurations of the bundles treated in the simulations: (A) a bundle of six (10,10) SWNTs; (B) a bundle of six DWNTs (10,10) inside a (15,15); (C) a bundle of three TWNTs (5,0) inside a (8,8) inside a (22,0).

The initial arrangement of the nanotubes in bundles in the simulations is shown in Figure 1. Every nanotube is 5.0 nm long and has 800, 1202, and 1940 atoms for SWNTs, double-walled nanotubes (DWNTs), and triple-walled nanotubes (TWNTs), respectively. The SWNTs considered are (10,10) nanotubes, the DWNTs are (5,5) nanotubes inside (10,10) nanotubes, and the TWNTs are (5,0) nanotubes inside (8,8) nanotubes that are inside (22,0) nanotubes. At the edge of every nanotube a layer that is 0.5 nm wide is subjected to Langevin frictional forces[41] to maintain the nanotubes at a constant temperature and mimic the heat dissipation properties of a real nanotube bundle. No other constrains are applied to the system. Periodic boundary conditions are applied in the direction of the nanotube axis to simulate nanotubes longer than 5 nm. The reported results are averages over 80 trajectories per incident energy for each nanotube bundle considered. Every trajectory was performed on a fresh bundle and configured so that the ions would be deposited at new locations on the bundle walls.

Computational Results

The computational results are summarized in Table 1 for the deposition of CH_3^+ ions on the nanotube bundles shown in Figure 1. At incident energies of 10 eV, only two kinds of phenomena are predicted. The first is elastic scattering of CH_3 from the nanotubes, and the second is chemical adsorption of CH_3 to the nanotube walls. At this energy, the simulations predict a high efficiency of functionalization through ion bombardment with 84%, 68%, and 80% of the impacting ions adhering to the outer walls of SWNTs, DWNTs, and TWNTs,

TABLE 1: Percentage of Events Taking Place in Collisions of CH_3^+ Ions with a Bundle of (10,10) SWNTs, Double-walled (5,5) and (10,10) MWNTs, and Triple-walled (5,0), (8,8), and (22,0) MWNTs[a]

	single wall			double wall			triple wall		
	10 eV	45 eV	80 eV	10 eV	45 eV	80 eV	10 eV	45 eV	80 eV
Scattering of C from nanotubes			0.4						0.4
Scattering of CH from nanotubes		3.3	2.5		9.2	2.1		2.1	2.9
Scattering of CH_2 from nanotubes		5.8	0.8		1.7			3.8	2.9
Scattering of CH_3 from nanotubes	16.3	2.5	1.25	31.7	5.8	1.7	20.0	7.9	
Adsorption of C on outside wall		1.3	17.5		2.1	14.2		2.1	5.8
Adsorption of CH on outside wall		26.2	15.8		27.9	13.3		23.3	12.5
Adsorption of CH_2 on outside wall		28.8	2.9		27.1	2.1		22.9	2.5
Adsorption of CH_3 on surface	83.7	2.1		68.3	2.5	0.4	80.0		
Incorporation of C, CH into outer wall with formation of defect structure forms		28.3	41.2		2.1	15.4		12.9	16.7
Sticking of C in inside wall or between walls		1.7	17.9		21.7	50.4		25.0	56.3

[a] The data are the average of the outcomes of 80 trajectories (240 collisions) performed for each incident energy.

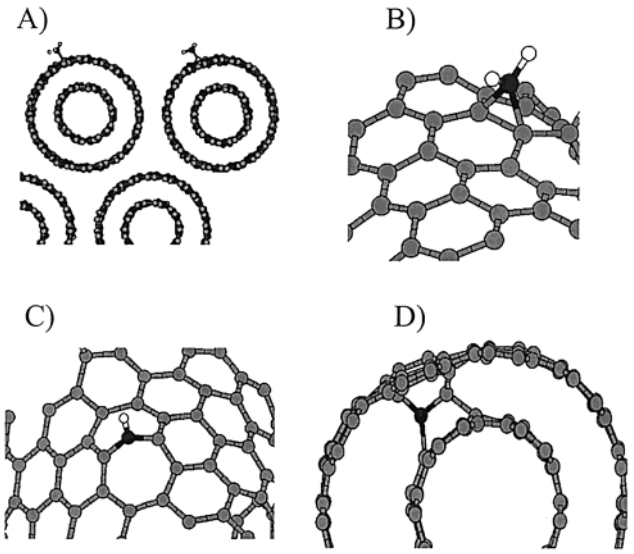

Figure 2. Snapshots from the molecular dynamics simulations after deposition of CH_3^+ ions on the bundles shown in Figure 1: (A) functionalization of DWNTs after deposition at 10 eV; (B) example of a functionalized SWNT wall after deposition at 45 eV; (C) example of two heptagon defects created after deposition at 45 eV; (D) intrashell cross-link formation in a DWNT after deposition at 45 eV.

respectively (see Figure 2A). No damage to the nanotube wall structure is predicted except for a very slight local deformation due to the change of the adsorptive site hybridization from sp^2 to sp^3 and the subsequent local change of bond lengths from 0.142 to 0.155 nm. At this low energy, the impacting ions do not probe the elasticity of the nanotubes (no deformation of the nanotube shape is observed for the SWNTs, DWNTs, or TWNTs), which is why there is almost no difference in the statistical range of error.

At 45 eV of incident energy, most of the ions lose one or two of their hydrogen atoms on impact. Most of the time (55% for SWNTs, 55% for DWNTs, and 46% for TWNTs), the larger fragments, such as CH and CH_2, adsorb on the outer surface of the targeted nanotube. Some of these fragments bond to two or three carbon atoms on the wall thus stabilizing the functional group at the surface (see Figure 2B). Less than 17% of the total number of fragments are reflected elastically from the walls for any of the nanotubes considered. Some of the time (~28% of the time for SWNTs, ~2% of the time for DWNTs, and ~13% for TWNTs), hydrocarbon fragments from the incident ions insert carbon atoms into the outer nanotube wall creating defects on the surface (usually in the form of a few heptagons as shown in Figure 2C).

The substantial difference in the percentage of defects created on the SWNTs versus those created on the MWNTs is explained by their different elastic properties. As was shown by several groups,[6,38,39] SWNTs are very elastic. They therefore deform easily on ion deposition (so that the amplitude of deformation at the strike can reach $^1/_3$ of it's diameter) and return to their prior shape with the same ease following deposition. In contrast, in the case of DWNTs and TWNTs, repulsive van der Waals interactions between the inner shells prevent easy deformation of the outer shell, thus effectively increasing the overall stiffness of the nanotube. This result has also been observed in studies of the ease with which nanotubes deform on surfaces.[42] Consequently, fewer of the impacting ions and fragments of ions are incorporated into the outer walls of the MWNTs. Instead, about 22% of time in the case of DWNTs and about 25% of the time in case of TWNTs, the impacting ions knock out one or two carbon atoms from the outer nanotube walls (compared with about a knockout rate of about 2% for SWNTs). This allows them to penetrate the wall and stick between the outer two nanotube walls, creating intrashell cross-links as shown in Figure 2D.

These defects on the outer nanotube walls and cross-links between walls (which are also, in some sense, defects) change the symmetry, electron hybridization, and π-bonding of the nanotubes and could therefore substantially alter the mechanical and electrical properties of the MWNTs. The influence of defects and geometrical deformation on electron transport properties of SWNTs has been studied theoretically.[43−46] The authors in ref 43 demonstrate that defects can substantially decrease conductance. In contrast, the authors in refs 44 and 45 are convinced that the effect of defects on electronic properties is relatively modest. Finally, the authors in ref 46 show that moderate deformations do not affect transport properties while large ones substantially decrease conductivity.

At 80 eV, very small percentages of ion fragments (~5% for SWNTs, ~4% for DWNTs, and ~6% for TWNTs) are scattered away after deposition. The remaining fragments adhere to the nanotube walls. In addition, most of the carbon atoms from the deposited species are inserted into the nanotube walls and create defects or end up underneath the outer wall or between walls. In other words, they would rather modify the internal structure of the nanotube walls than adsorb on the outside of (functionalize) the walls. The total amount of atoms and fragments adsorbed on the surface of the nanotubes (chemical functionalization) is 36% for SWNTs, 30% for DWNTs, and 21% for TWNTs. The total amount of atoms and fragments incorporated within or under the surface (between two walls) is 59% for SWNTs, 65% for DWNTs, and 73% for

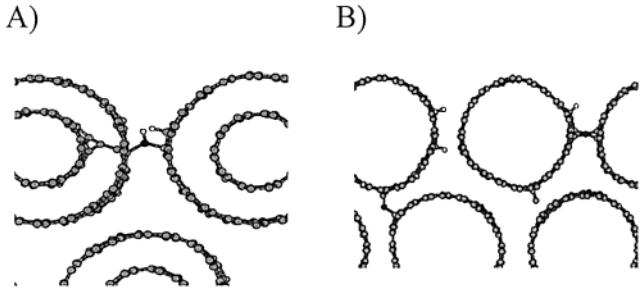

Figure 3. Examples of cross-linking between nanotubes in a bundle as a result of ion bombardment: (A) SWNT; (B) DWNT.

TWNTs. Therefore, most of the incident energy is directed to modification of the inner sections of the nanotubes rather than to functionalization of their outer layers.

At this energy, the simulations indicate significant differences in the results for SWNTs and MWNTs as a result of the difference in their elastic properties for the same reasons discussed above for the 45 eV impacts. For SWNTs, ~41% of the fragments are incorporated into the walls in the form of defects and ~18% stick inside of the outer wall. For MWNTs, 15−17% of fragments are incorporated into the outer walls in the form of defects and 50−56% of the fragments stick between the walls. In rare cases (~2.5% of the time), the carbon atom knocked out of the outer wall by the incoming ion is able to knock subsequent carbon atoms out of the second wall and replace them (see Figure 3A). The carbon atom from the inner wall is then adsorbed under the inner shell or, in case of the TWNTs, between the second and third shells. Besides the junctions between the shells of the same nanotube at this energy, the simulations predict adsorption of hydrocarbon fragments or single atoms between different nanotubes in the bundle with the creation of internanotube cross-links in the case of both SWNT and MWNT bundles (see Figure 3B).

The first reason for adhesion of carbon atoms between nanotubes is explained by the effective knocking out of carbon atoms by the impacting ions. Because the incoming ions are very close in mass to the carbon atoms of the nanotube, the transfer of momentum is very effective and knocked-out atoms could in their turn knock out carbon atoms from the layer underneath. These knocked-out carbon atoms then stick between the first and second shells of the nanotubes. Such events usually occur at strikes that are close to the central part of the SWNTs. In addition, high-velocity collisions remove hydrogen atoms from the impacting ions, thus releasing the valence electrons that are necessary to attach the two nanotubes. These events usually happen at strikes on the sides of the nanotubes. The formation of covalent bonding between nanotubes in ordered bundles is also predicted at high pressure by ab initio simulations.[47]

Finally, to examine the issue of effective formation of junctions between neighboring nanotubes, the angular bombardment of crossed nanotubes by a beam (36 atoms) of low-energy carbon ions is considered (see Figure 4A). At incident energies of 3 eV, the simulations predict the formation of multiple carbon chains connecting the two SWNT (as shown in Figures 4B and 4C). However, little additional nanotube damage and few other defect structures are predicted to form at this energy. The crossing of nanotubes has attracted attention because the crossed structure may function as a basic electrical circuit.[28−30] For example, it has been shown[29] that electrical transport properties through crossed nanotubes that are separated by 0.34 nm have tunneling character (i.e., an electron arriving at the junction in one SWNT has a probability of a few percent of tunneling through the barrier to the other SWNT). The measurements performed[30] for crossed nanotubes support the bulk-to-bulk tunneling character of electron transport and show that conductance of this structure at room temperature is 3 orders of magnitude less than the quantum conductance 4 e^2/h or even the one for a regular nanotube. It is supposed that the intertube junctions formed by ion fragments between nanotubes could substantially reduce or even remove this tunnel barrier.

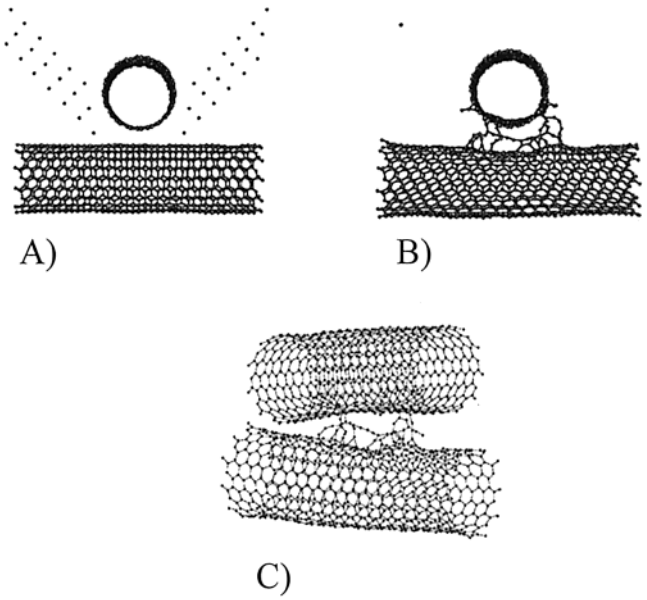

Figure 4. Example of junctions between two crossed SWNTs formed as a result of directed ion bombardment: (A) initial configuration; (B) side view of resulting junctions; (C) angled view of resulting junctions.

Experimental Results

The only elements observed in the X-ray photoelectron spectroscopy (XPS) survey scans of the native MWNT samples are carbon and iron. Iron exists as a few percentage impurity from the nanotube synthesis step (data not shown). Figure 5 (lower traces) displays the core level XPS of the F(1s) and C(1s) regions of the native nanotubes. No fluorine is observed on the native nanotubes. The C(1s) region displays a primary C peak referenced to a binding energy of 285.0 eV. This C peak is unusually narrow, with an instrumental resolution limited width of 0.7 eV, because of the predominance of only aromatic carbon in the nanotubes. By contrast, the C(1s) peak of clean polystyrene displays a width of 0.95 eV because of the presence of both aromatic and aliphatic carbon.[32] The C(1s) region of the native nanotubes also displays a prominent $\pi-\pi^*$ transition, centered at a binding energy of ~292 eV, with a width of ~3.5 eV.

The XPS survey scans of the 45 eV CF_3^+ ion-modified nanotubes show peaks due to carbon, fluorine, and the slight iron impurity (not shown, see above). Figure 5 (upper traces) displays the core level XPS of the F(1s) and C(1s) regions of the 45 eV CF_3^+ ion-modified nanotubes. The F(1s) peak displays a 695 eV binding energy and does not display any structure, as is typical for fluorocarbons.[32] Table 2 shows that the 10, 10 (high dose), and 45 eV CF_3^+ ion-modified nanotube samples have 22, 33, and 29% fluorine, with the remainder carbon (ignoring the small iron impurity in the native samples).

The C(1s) peak of the 45 eV ion-modified nanotubes in Figure 5 (upper trace) displays several components that can be attributed to the following fluorocarbon components (detected

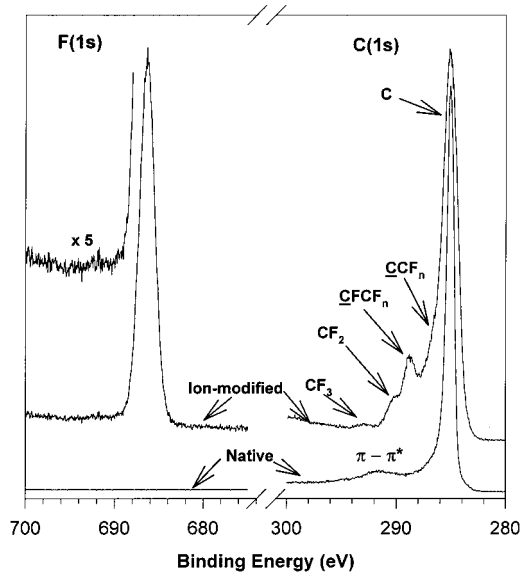

Figure 5. The core level X-ray photoelectron spectra (XPS) of the F(1s) and C(1s) regions for the native, unmodified nanotubes (lower traces) and the F(1s) and C(1s) XPS for 45 eV CF_3^+ ion-modified nanotubes, prepared with regular ion dose (upper traces).

TABLE 2: Chemical Composition of Native and CF_3^+ Ion-modified Nanotubes, in Percent[a]

component/ binding energy, eV (fwhm)	native	10 eV CF_3^+ (5×10^{15} ions/cm^2)	10 eV CF_3^+ (1×10^{16} ions/cm^2)	45 eV CF_3^+ (5×10^{15} ions/cm^2)
C/285.0 (0.70[b] or 0.95[c])	92	54 ± 1	41 ± 1	48 ± 2
*C*CF$_n$/286.2 (1.9)		35 ± 1	44 ± 1	33 ± 3
*C*FCF$_n$/288.7 (1.8)	3 ($\pi-\pi^*$)[e]	3.7 ± 0.5	5.5 ± 0.4	10.5 ± 0.3
CF$_2$/291.7 (1.4)	3 ($\pi-\pi^*$)[e]	3.7 ± 0.5	4.5 ± 0.4	6.3 ± 0.8
CF$_3$/293.3 (1.4)	1 ($\pi-\pi^*$)[e]	2.8 ± 0.3	4.2 ± 0.2	2.4 ± 0.2
total carbon[d]	100	80 ± 2	67 ± 1	71 ± 2
total fluorine[d]	0	22 ± 2	33 ± 1	29 ± 2

[a] Data from deconvolution of C(1s) peak and F(1s)/C(1s) ratio of X-ray photoelectron spectra. [b] fwhm of C(1s) on native nanotubes. [c] fwhm of C(1s) on ion-modified nanotubes. [d] Does not take into account a slight iron impurity of a few percent. [e] The "fluorocarbon" components in the native nanotube sample are actually due to the broad (~3.5 eV fwhm) $\pi-\pi^*$ transition on the C(1s) peak.

C atom shown in italics): C, *C*CF$_n$, *C*FCF$_n$, CF$_2$, and CF$_3$.[32] Table 2 displays the binding energies, widths (fwhm), and percentages of these fluorocarbon components. The $\pi-\pi^*$ transition of the native nanotubes overlaps with several of the C(1s) peaks of fluorinated carbon. This transition is compensated for in the Figure 6 bar graphs by subtracting the $\pi-\pi^*$ component (obtained by fitting the native nanotube $\pi-\pi^*$ peak to the fluorocarbon peak positions and widths noted in Table 2) from the fluorocarbon peaks of the ion-modified samples.

Figure 6 further shows that the percentage of the CF_3 component is greatest following high-dose 10 eV deposition and negligible following 45 eV deposition. This component corresponds to intact CF_3 that adsorbs to or implants intact within the nanotube walls. These experimental results roughly agree with the simulations (see Table 1), which predicted that adsorption of CH_3 on the nanotube surface is dominant at 10 eV but is only a minor channel at higher deposition energies.

Figure 6 also shows that the *C*FCF$_n$ and CF$_2$ components are highest following 45 eV CF_3^+ deposition. These components correspond to a reaction channel predicted by the 45 eV simulations: adsorption of CF and CF$_2$ on the nanotube wall or incorporation of CF into the wall.

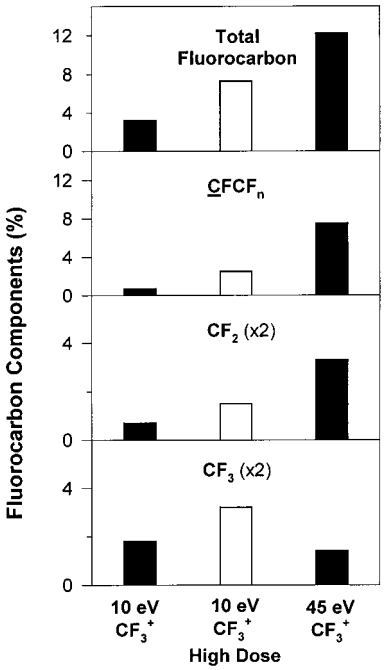

Figure 6. Bar graph of individual and total fluorocarbon components for 10 and 45 eV CF_3^+ ion-modified nanotubes at regular and high ion dose. Data are taken from Table 2, after subtracting out contributions of $\pi-\pi^*$ transitions of native nanotubes. Total fluorocarbon is sum of *C*FCF$_n$, CF$_2$, and CF$_3$ components only (not *C*CF$_n$).

The regular-dose 10 eV data also display only small CF$_2$ and *C*FCF$_n$ components, but these become more significant for the high-dose experiment. This contrasts with the 10 eV simulations, which only displayed adsorption of intact CH_3. However, the simulations of 3 eV bombardment of crossed nanotubes did show carbon chain junctions forming between adjacent tubes (see Figure 4). That these CF$_2$ and *C*FCF$_n$ components increase from the low- to high-dose experiments at 10 eV supports the formation of either carbon chain junctions (which could not be composed solely of CF_3) or a thicker fluorocarbon overlayer. Alternatively, these CF$_2$ and *C*FCF$_n$ components might be due to longer term reactions that convert adsorbed CF_3 into CF$_2$ and CF but whose longer time scale cannot be simulated here.

The total fluorocarbon depicted in the top of Figure 6 is defined here as the sum of the *C*FCF$_n$, CF$_2$, and CF$_3$ components (after subtraction of the $\pi-\pi^*$ transition and not including the *C*CF$_n$ component). The total fluorocarbon is largest for the 45 eV sample, whereas the total fluorine is greatest for the high-fluence 10 eV sample. This total fluorine versus fluorocarbon discrepancy is attributed to different film morphologies, as modulated by the different inelastic mean free paths of the C(1s) and F(1s) photoelectrons.

The 33−44% *C*CF$_n$ component observed in all three modified samples (see Table 2) can be attributed to the carbon atoms on the nanotubes that are adjacent to sticking/implanted CF$_x$ species. A portion of the *C*CF$_n$ and *C*FCF$_n$ components might actually be attributed to an unresolved *C*F−C$_n$ component, which would be expected to appear at the intermediate binding energy of ~287.2 eV.[32]

The above interpretation argues for nanotubes that are functionalized or implanted with CF$_x$ groups. CF$_x$ functionalized/implanted nanotubes would be expected to continue to display the strong $\pi-\pi^*$ transition near 292 eV seen for the native nanotubes. The $\pi-\pi^*$ subtraction employed in Figure 6 conservatively assumes that the nanotubes maintain their aromatic nature upon CF_3^+ modification and will lead to an

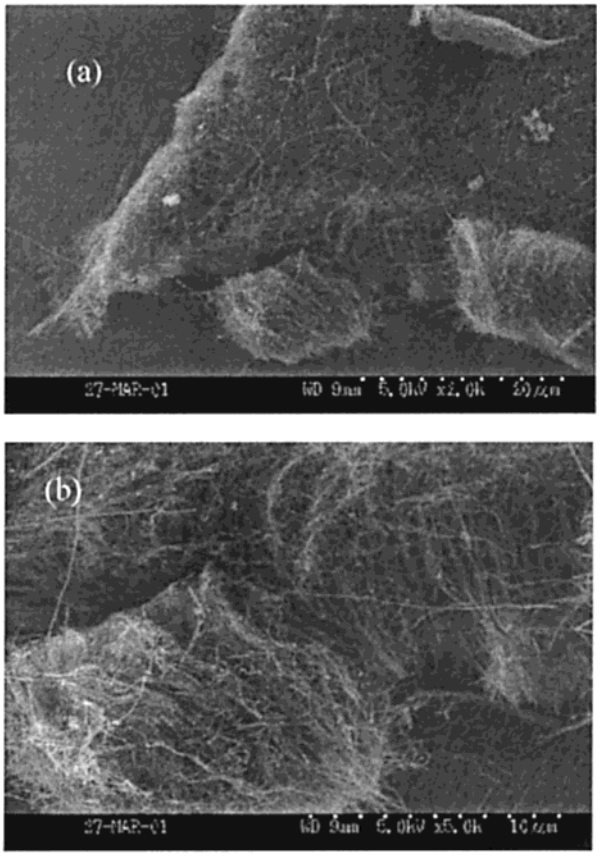

Figure 7. SEM images of nanotubes (a) near the bombardment site and (b) distant to the bombardment site. No changes in nanotube morphology indicative of physical damage are evident.

underestimation of the total fluorocarbon. However, similar spectra would be observed from a highly cross-linked, relatively thick fluorocarbon overlayer.[32] Such thick overlayers have been formed on nanotubes from plasma activation.[48] The $\pi-\pi^*$ transition would be reduced or disappear altogether for these overlayers or if ion bombardment lead to significant decomposition of the nanotube structure.

Scanning electron microscopy is therefore used to inspect the nanotube array for thick overlayer formation or morphological damage caused during ion bombardment. Nanotubes from the site of bombardment (a ~5−8 mm dot in the center of the Si wafer) and from sites around this location were removed and mounted for SEM analysis. Nanotubes distant from the bombardment site (from near the plaque edge) were used for comparison. As illustrated in Figure 7, no obvious change in the nanotube morphology has occurred under ion bombardment, suggesting that little or no gross physical damage is done to the nanotubes by this process and confirming that the XPS analysis is from nanotubes rather than a thick, cross-linked fluorocarbon film. The nanotubes were not sputtered prior to SEM so that any gross roughing of the surface or exfoliation of the outer shells would have been evident.

Discussion and Conclusions

This combined experimental and computational study of low-energy ion-beam modification of carbon nanotube bundles indicates that ion beams can be used to functionalize, cross-link, connect, and create defect structures in the nanotubes. This process might therefore be used to create covalent connectors between crossed nanotubes for use in electronic devices. It might also be used to chemically functionalize the nanotubes so that they may eventually be solubilized or made to adhere more strongly to the matrix in a composite material. It is expected that the defects created on the nanotube walls would heal on time scales longer than those accessible through molecular dynamics simulations. However, it also expected that they will not be removed completely. They could therefore act as preferred sites for further chemical reactions as has been discussed in the literature.[48,49]

The predicted cross-linking between nanotube walls and neighboring nanotubes could fundamentally alter the mechanical and electrical properties of the nanotubes or nanotube bundles. For example, bundled nanotubes connected by cross-linked groups would be expected to be more resistant to shear forces than bundled nanotubes with no cross-linking groups. It should be pointed out, however, that this toughening would be expected to be limited to nanotubes at the surface of the bundle.

With regard to the effects on electronic properties, the electronic transport properties of MWNTs have been studied extensively. For instance, it has been demonstrated[50] that the conductance of MWNTs is quantized and does not depend on the number of shells. This leads to the conclusion that electrical conductance in MWNTs is provided by the outer layer only, which is partly supported by other studies.[51,52] In these papers, it was shown that DWNT layers preserve the basic properties of the uncoupled nanotubes. Interlayer coupling in these studies is accepted to be much weaker (by an order of magnitude) than intralayer ones corresponding to van der Waals distances between layers. However, these studies have been restricted by theoretical consideration of particular cases of metallic−metallic and metallic−semiconducting DWNTs. It would be worthwhile to study the conductive properties of MWNTs with intralayer junctions in comparison with ones without them. We suppose that the conductive properties of MWNTs with junctions could be dependent on the chirality of the outer and inner layers and might be analogous to end-to-end junctions of two SWNT with different chiralities. It has been demonstrated[23−27] that SWNTs connected at the ends through pentagon−heptagon defects have semiconducting electrical properties. The exact manner in which the conductance of MWNTs would depend on intralayer junctions is the subject of current investigations.

Acknowledgment. This work was supported by the National Science Foundation through the following grants: Grant NSF-CHE-9708049 (S.B.S.), the Advanced Carbon Materials Center through Grant NSF-DMR-9809686 (S.B.S., R.A., and D.J.), the Particle Science and Technology Center through Grant NSF-EEC-9402989 (S.B.S.), and Grant NSF-CHE-9986226 (L.H.).

References and Notes

(1) Mintmire, J. W.; Dunlap, B. I.; White, C. T. *Phys. Rev. Lett.* **1992**, *68*, 631.
(2) Tans, S. J.; Devoret, M. H.; Dai, H.; Thess, A.; Smalley, R. E.; Geerligs, L. J.; Dekker, C. *Nature* **1997**, *386*, 474.
(3) Bockrath, M.; Cobden, D. H.; McEuen, P. L.; Chopra, N. G.; Zettl, A.; Thess, A.; Smalley, R. E. *Science* **1997**, *275*, 1922.
(4) Martel, R.; Schmidt, T.; Shea, H. R.; Hertel, T.; Avouris, P. *Appl. Phys. Lett.* **1998**, *73*, 2447.
(5) Tans, S. J.; Devoret, M. H.; Groeneveld, R. J. A.; Dekker, C. *Nature* **1998**, *393*, 49.
(6) Yakobson, B. I.; Brabec, C. J.; Bernholc, J. *Phys. Rev. Lett.* **1996**, *76*, 2511.
(7) Krishnan, A.; Dujardin, E.; Ebbesen, T. W.; Yianilos, P. N.; Treacy, M. M. J. *Phys. Rev. B* **1998**, *58*, 14013.
(8) Yao, N.; Lordi, V. *J. Appl. Phys.* **1998**, *84*, 1939.
(9) Ebbesen, T. W.; Ajayan, P. M.; Hiura, H.; Tanigaki, K. *Nature* **1994**, *367*, 519.
(10) Bandow, S.; Rao, A. M.; Williams, K. A.; Thess, A.; Smalley, R. E.; Eklund, P. C. *J. Phys. Chem. B* **1997**, *101*, 8839.

(11) Shelimov, K. B.; Esenaliev, R. O.; Rinzler, A. G.; Huffman, C. B.; Smalley, R. E. *Chem. Phys. Lett.* **1998**, *282*, 429.
(12) Mizoguti, E.; Nihey, F.; Yudasaka, M.; Iijima, S.; Ichihashi, T.; Nakamura, K. *Chem. Phys. Lett.* **2000**, *321*, 297.
(13) Andrews, R.; Jacques, D.; Qian, D.; Dickey, E. C. *Carbon* **2001**, *39*, 1681.
(14) Chen, Y.; Haddon, R. C.; Fang, S.; Rao, A. M.; Eklund, P. C.; Lee, W. H.; Dickey, E. C.; Grulke, E. A.; Pendergrass, J. C.; Chavan, A.; Haley, B. E.; Smalley, R. E. *J. Mater. Res.* **1998**, *13*, 2423.
(15) Chen, J.; Hamon, M. A.; Hu, H.; Chen, Y.; Rao, A. M.; Eklund, P. C.; Haddon, R. C. *Science* **1998**, *282*, 95.
(16) Seifert, G.; Kohler, T.; Frauenheim, T. *Appl. Phys. Lett.* **2000**, *77*, 1313.
(17) Wong, S. S.; Joselevich, E.; Woolley, A. T.; Cheung, C. L.; Lieber, C. M. *Nature* **1998**, *394*, 52.
(18) Wong, S. S.; Woolley, A. T.; Joselevich, E.; Cheung, C. L.; Lieber, C. M. *J. Am. Chem. Soc.* **1998**, *120*, 8557.
(19) Mickelson, E. T.; Huffman, C. B.; Rinzler, A. G.; Smalley, R. E.; Hauge, R. H.; Margrave, J. L. *Chem. Phys. Lett.* **1998**, *296*, 188.
(20) Mickelson, E. T.; Chiang, I. W.; Zimmerman, J. L.; Boul, P. J.; Lozano, J.; Liu, J.; Smalley, R. E.; Hauge, R. H.; Margrave, J. L. *J. Phys. Chem. B* **1999**, *103*, 4318.
(21) Boul, P. J.; Liu, J.; Mickelson, E. T.; Huffman, C. B.; Ericson, L. M.; Chiang, I. W.; Smith, K. A.; Colbert, D. T.; Hauge, R. H.; Margrave, J. L.; Smalley, R. E. *Chem. Phys. Lett.* **1999**, *310*, 367.
(22) Ni, B.; Sinnott, S. B. *Phys. Rev. B* **2000**, *61*, R16343.
(23) Yao, Z.; Postma, H. W. C.; Balents, L.; Dekker, C. *Nature* **1999**, *402*, 273.
(24) Saito, R.; Dresselhaus, G.; Dresselhaus, M. S. *Phys. Rev. B* **1996**, *53*, 2044.
(25) Chico, L.; Crespi, V. H.; Benedict, L. X.; Louie, S. G.; Cohen, M. L. *Phys. Rev. Lett.* **1996**, *76*, 971.
(26) Tamura, R.; Tsukada, M. *Phys. Rev. B* **1997**, *55*, 4991.
(27) Ferreira, M. S.; Dargam, T. G.; Muniz, R. B.; Latge, A. *Phys. Rev. B* **2000**, *63*, 16040.
(28) Lefebvre, J.; Lynch, J. F.; Llaguno, M.; Radosavljevic, M.; Johnson, A. T. *Appl. Phys. Lett.* **1999**, *75*, 3014.
(29) Fuhrer, M. S.; Nygard, J.; Shih, L.; Forero, M.; Yoon, Y.-G.; Mazzoni, M. S. C.; Choi, H. J.; Ihm, J.; Louie, S. G.; Zettle, A.; McEuen, P. L. *Science* **2000**, *288*, 494.
(30) Postma, H. W. C.; Jonge, M. d.; Yao, Z.; Dekker, C. *Phys. Rev. B* **2000**, *62*, R10653.
(31) Andrews, R.; Jacques, D.; Rao, A. M.; Derbyshire, F.; Qian, D.; Fan, X.; Dickey, E. C.; Chen, J. **1999**, *303*, 467.
(32) Wijesundara, M. B. J.; Ji, Y.; Ni, B.; Sinnott, S. B.; Hanley, L. *J. Appl. Phys.* **2000**, *88*, 5004.
(33) Wijesundara, M. B. J.; Hanley, L.; Ni, B.; Sinnott, S. B. *Proc. Natl. Acad. Sci. U.S.A.* **2000**, *97*, 23.
(34) Scofield, J. H. *J. Electron Spectrosc. Relat. Phenom.* **1976**, *8*, 129.
(35) Brenner, D. W. *Phys. Status Solidi B* **2000**, *217*, 23.
(36) Sinnott, S. B.; Shenderova, O. A.; White, C. T.; Brenner, D. W. *Carbon* **1998**, *36*, 1.
(37) Yakobson, B. I.; Campbell, M. P.; Brabec, C. J.; Bernholc, J. *Comput. Mater. Sci.* **1997**, *8*, 341.
(38) Garg, A.; Han, J.; Sinnott, S. B. *Phys. Rev. Lett.* **1998**, *81*, 2260.
(39) Cornwell, C. F.; Wille, L. T. *Solid State Commun.* **1997**, *101*, 555.
(40) Claire, P. D. S.; Son, K.; Hase, W. L.; Brenner, D. W. *J. Am. Chem. Soc.* **1996**, *100*, 1761.
(41) Allen, M. P.; Tildesley, D. J. *Computer Simulation of Liquids*; Oxford University Press: New York, 1987.
(42) Hertel, T.; Walkup, R. E.; Avouris, P. *Phys. Rev. B* **1998**, *58*, 13870.
(43) Kostyrko, T.; Bartkowiak, M.; Mahan, G. D. *Phys. Rev. B* **1999**, *60*, 10735.
(44) Orlikowski, D.; Nardelli, M. B.; Bernholc, J.; Roland, C. *Phys. Rev. B* **2000**, *61*, 14194.
(45) Nardelli, M. B. *Phys. Rev. B* **1999**, *60*, 7828.
(46) Hansson, A.; Paulsson, M.; Stafstrom, S. *Phys. Rev. B* **2000**, *62*, 7639.
(47) Yildirim, T.; Gulseren, O.; Kilic, C.; Ciraci, S. *Phys. Rev. B* **2000**, *62*, 12648.
(48) Chen, Q.; Dai, L.; Gao, M.; Huang, S.; Mau, A. *J. Phys. Chem. B* **2001**, *105*, 618.
(49) Srivastava, D.; Brenner, D. W.; Schall, J. D.; Ausman, K. D.; Yu, M.; Ruoff, R. S. *J. Phys. Chem. B* **1999**, *103*, 4330.
(50) Frank, S.; Poncharal, P.; Wang, Z. L.; Heer, W. A. d. *Science* **1998**, *280*, 1744.
(51) Saito, R.; Dresselhaus, G.; Dresselhaus, M. S. *J. Appl. Phys.* **1993**, *73*, 494.
(52) Lambin, P.; Meunier, V.; Rubio, A. *Phys. Rev. B* **2000**, *62*, 5129.